Optical model and coupled-channels analyses of the elastic and inelastic scattering of ^{18}O from ^{28}Si at 352 MeV

B. L. Burks, M. A. G. Fernandes,* G. R. Satchler, D. J. Horen, F. E. Bertrand, J. L. Blankenship, J. L. C. Ford, Jr.,† E. E. Gross, D. C. Hensley, R. O. Sayer, D. Shapira, and T. P. Sjoreen
Oak Ridge National Laboratory, Oak Ridge, Tennessee 37831
(Received 27 May 1988)

Differential cross sections have been measured for the elastic and inelastic scattering of ^{18}O from ^{28}Si at 352 MeV. An optical model analysis has been performed for the elastic scattering data. Considerable ambiguity was found. Potentials which are either transparent or strongly absorbing in the surface region were obtained which give equally good fits to the data. The combined elastic and inelastic data were subjected to a coupled-channels analysis and the ambiguity was found to persist, in contrast to previously reported one-nucleon transfer data whose analysis allowed us to discriminate between the two types of potential. Other characteristics of the scattering are discussed.

I. INTRODUCTION

The results of optical-model analyses of heavy-ion elastic scattering are often ambiguous because of the strong absorption which is present. Frequently, the ambiguity is almost complete at low incident energies E, not far above the Coulomb barrier (typically $E/A \lesssim 10$ MeV). Then one determines[1-3] mainly the values of the real and imaginary parts of the potential in the vicinity of some strong absorption radius R_{SA} (typically $R_{SA} \approx [1.1(A_1^{1/3}+A_2^{1/3})+2.7]$ fm), perhaps with some constraints upon the potential slopes in this region. At higher energies (e.g., $E/A \gtrsim 20$ MeV), the projectile and target nuclei may approach more closely before complete absorption occurs and, in principle, one may learn more about the potential in this surface region. Even then, however, the potential may not be determined uniquely because this requires either very precise measurements at forward angles, or the accurate measurement of very small cross sections at larger angles.

The work presented here provides another example of this situation for $^{18}O+^{28}Si$ at $E/A=19.54$ MeV. We have reported elsewhere[4] that the analysis of one-nucleon transfer data, measured in the same experiment, enables us to resolve clearly at least one kind of optical potential ambiguity. Here we examine the ambiguities in more detail and we also show that they cannot be resolved by considering the results of the inelastic measurements.

We distinguish between two kinds of ambiguities. One is a parameter ambiguity that arises because the functional form chosen (e.g., Woods-Saxon) is able, in the radial region to which the scattering is sensitive, to reproduce the same potential with a wide range of parameter values. A well-known example is the Igo ambiguity.[5] The other kind of ambiguity, with which we are more concerned in the present work, is between conventional strong-absorption potentials ($\mathrm{Im}\,|U| \gtrsim \mathrm{Re}\,|U|$ in the surface) and surface-transparent ones (a surface region with $\mathrm{Im}\,|U| < \mathrm{Re}\,|U|$ surrounding a strongly absorbing core). These two kinds of potentials result in different (complex) phase shifts, but the elastic cross sections are sufficiently similar in the limited angular region usually covered experimentally, that typical measurements are unable to distinguish clearly between them. This ambiguity is also related to the two extreme interpretations,[1,2] Fresnel (diffractive) or Coulomb-rainbow (refractive) often applied to heavy-ion scattering at the lower energies.

A typical example of these ambiguities is provided by analyses[6,7] of measurements on $^{16}O+^{28}Si$ scattering, which has been studied over a wide range of bombarding energies up to 215 MeV. Many of the data were confined to limited angular ranges in the forward direction. Extending the measurements to larger angles should help to resolve the ambiguities. When this was done[8] at energies of $E/A \lesssim 3.5$ MeV, including angles close to 180°, ambiguity remained, but it was established[8,9] that the potential at these low energies was characterized by some surface transparency which allowed relatively large cross sections for scattering to 180°.

In the present work, we examine the scattering of the adjacent system $^{18}O+^{28}Si$. We present results for elastic and inelastic scattering at a bombarding energy of 352 MeV ($E/A=19.5$ MeV). These data, together with earlier results obtained[10] at 56 MeV ($E/A=3.1$ MeV, are subjected to optical-model and coupled-channels analyses. Potentials with various forms (Woods-Saxon, Woods-Saxon-squared and folded) were used. A farside/nearside decomposition[11] of the corresponding scattering was performed and used to help in the interpretation of the results.

During this experiment measurements were also made of the single-nucleon transfer[12] reactions $^{28}Si(^{18}O,^{17}O)^{29}Si$ and $^{28}Si(^{18}O,^{19}F)^{27}Al$ and the charge-exchange[13] reaction $^{28}Si(^{18}O,^{18}F)^{28}Al$. The respective results and their analyses have been presented elsewhere.[12,13] We note, in particular, that a description of the nucleon transfer reactions in terms of the distorted-wave Born approximation provided strong evidence[4] against the validity of using a surface-transparent potential at this energy, even though, as we shall show, it cannot be ruled out on the basis of

the elastic or inelastic measurements alone.

Experimental details and results are presented in Sec. II. The optical-model analyses of the elastic scattering data are described in Sec. III. Finally, in Sec. IV are discussed the results of a coupled-channel treatment of the measured elastic and inelastic angular distributions.

II. EXPERIMENTAL PROCEDURE AND RESULTS

The experiment was carried out with a 352 MeV ^{18}O beam from the coupled tandem and cyclotron accelerators at the Holifield Heavy Ion Research Facility (HHIRF). A self-supporting natural silicon target (92.2% ^{28}Si) with a thickness of $\sim 160\ \mu g/cm^2$ was used. The scattered particles were momentum analyzed in the HHIRF broad-range spectrograph (BRS) equipped with a vertical drift chamber (VDC) at the focal plane followed by a parallel-plate avalanche counter (PPAC) and a segmented-anode ionization chamber. This detector system,[14,15] allows both focal plane position and scattering angle measurement as well as charge and mass identification. The elastic and inelastic scattering data were acquired using five settings of the BRS magnetic field. The angular acceptance was approximately 4° at each setting. The data were obtained with ample overlap in angle to permit reliable internormalization of the measured cross sections taken at different field and angle settings. Since the angular distributions for both the inelastic scattering cross sections and the ratio of elastic scattering cross section to the Rutherford scattering cross section are highly oscillatory over much of the measured angular range, it is necessary to determine the cross sections in small angle bins. The angular resolution of the VDC at the focal plane corresponds to less than 0.1° in scattering angle at the target allowing extraction of the elastic and inelastic angular distributions in 0.16° bins over the angular range $2.6° \leq \theta_{lab} \leq 14.1°$. For the elastic data, the measurements were later extended to $\theta_{lab} \sim 18°$ in 0.5° bins. The overall energy resolution was $\simeq 220$ keV (FWHM) with the dominant contribution arising from straggling in the target.

Differential cross sections were determined from the measured target thickness and integrated beam current. An uncertainty of $\pm 10\%$ is estimated in the absolute cross sections attributed to uncertainties in measurements of the target thickness and of the charge collection.

In Fig. 1 is shown the focal plane position spectrum of ^{18}O scattering on ^{28}Si at $\theta_{lab} = 6.6°$. The elastic differential cross sections are displayed in Figs. 2 and 3. The structure located near channel 1200 in the spectrum represents excitations of the first 2^+ states in ^{28}Si (1.78 MeV) and ^{18}O (1.98 MeV). The yields for these two groups were extracted using a Gaussian peak-fitting routine. Cross sections were also determined for the peak near channel 1080 which corresponds to excitations of the 3^- level at 6.88 MeV in ^{28}Si. These inelastic cross sections are discussed in Sec. IV. Other structures in the spectrum correspond to mutual excitation of the first 2^+ states in ^{18}O and ^{28}Si (channel 1150), and states in ^{28}Si at 4.62 MeV (4^+), 7.42 MeV (2^+), and 10.18 MeV (3^-).

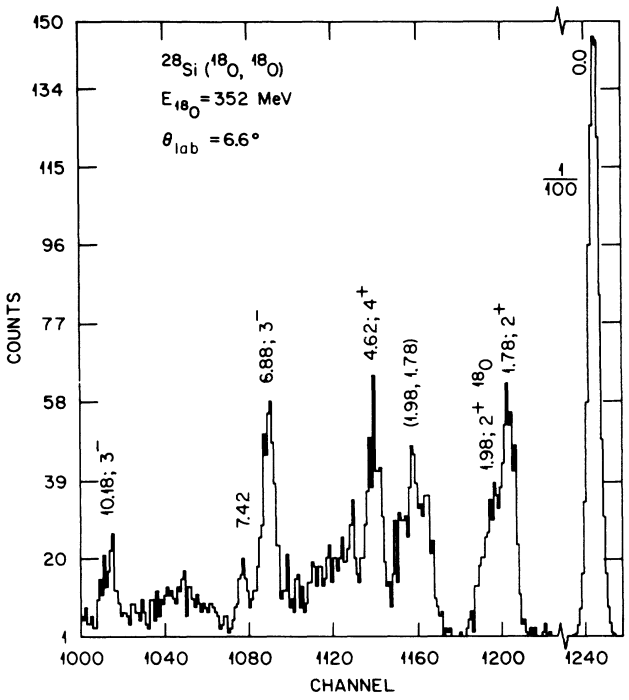

FIG. 1. Energy spectrum of the elastic and inelastic scattering of 352 MeV ^{18}O on ^{28}Si at $\theta_{lab} = 6.6°$.

III. OPTICAL-MODEL ANALYSIS OF ELASTIC SCATTERING

A. Introduction

Our approach to the analysis of the elastic cross sections for $^{18}O + ^{28}Si$ obtained in the present experiment was guided by previous work on the adjacent system

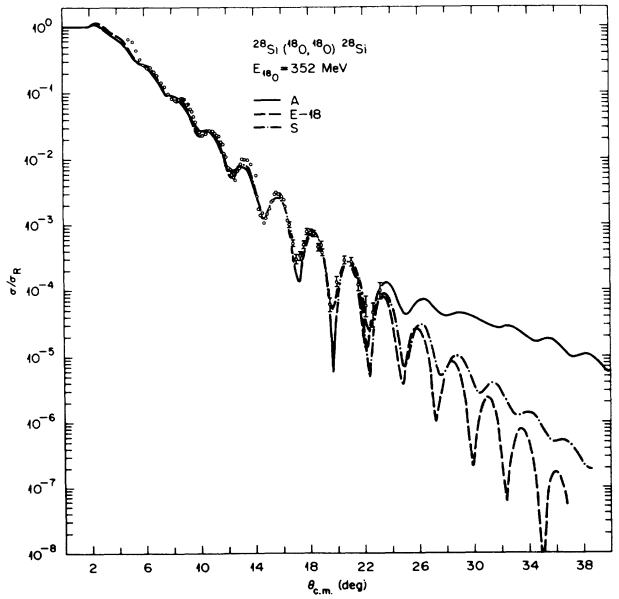

FIG. 2. $^{18}O + ^{28}Si$ elastic cross sections, in ratio to the Rutherford ones. The data are from the original measurements which did not extend beyond 23°. The curves are optical-model fits as described in the text, with parameter values given in Table I.

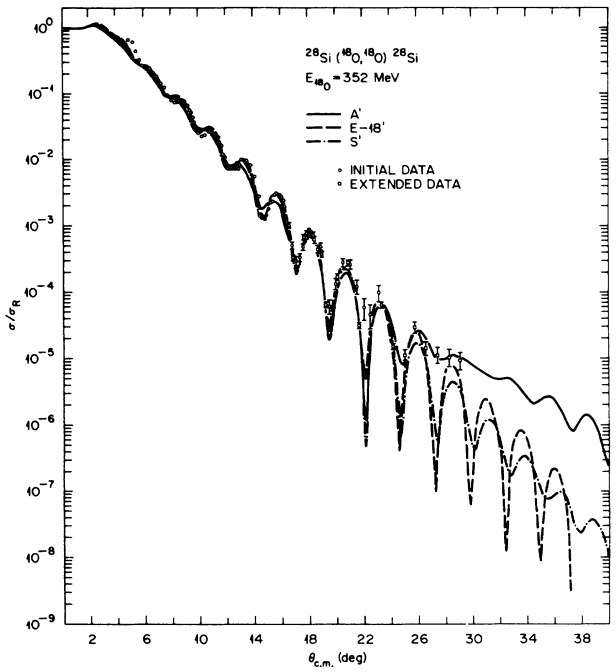

FIG. 3. Optical-model fits to the elastic cross sections which include the later measurements that extended back to 29°. The potential parameters are given in Table I.

^{16}O+^{28}Si. Several interesting features emerged from the latter studies and it is useful to compare them with the present results for ^{18}O scattering. For this purpose we also reanalyzed the ^{18}O data obtained earlier[10] at 56 MeV.

In one "global" study[6] of ^{16}O scattering, elastic data for 11 bombarding energies between 33 and 215 MeV were fitted simultaneously in order to find an energy-independent six-parameter potential of Woods-Saxon (WS) form

$$U(r)=-Vf(x_v)-iWf(x_w)\ , \tag{3.1a}$$

$$f(x)=(e^x+1)^{-1},\quad x=(r-R)/a\ . \tag{3.1b}$$

It was concluded that imposing the constraint of energy-independence leads uniquely to a shallow potential, the so-called E-18, with a real depth $V\simeq 10$ MeV and whose imaginary part is deeper ($W\approx 23$ MeV) but confined to somewhat smaller radii so that it is "surface transparent."[11] (The parameter values for this potential are included in Table I for reference purposes.)

It was later shown[7] that equally good fits could be obtained with a variety of other potentials with energy-independent real parts, including one with a very deep (~ 700 MeV) real part generated by the folding model,[16] provided the diffuseness of the imaginary parts were al-

TABLE I. Optical-model parameters for elastic scattering. Parameter values with underbars were not varied during the search. The Coulomb potential between two uniform charges (Ref. 19) of radii 3.68 and 4.05 fm was included except for the A, A' potentials where a point plus uniform charge with radius parameter $r_c=1.3$ fm was used.

Type	Energy (MeV)	V (MeV)	r_V[a] (fm)	a_V (fm)	W (MeV)	r_W[a] (fm)	a_W (fm)	σ_A (mb)	L_F[b] ($\hbar$)	D_F[b] (fm)	L_R[c] ($\hbar$)	$-\theta_R$[c] (deg)
F	352	$N=0.524$[d]			277.4	0.7	0.946	2354	76.5	7.7	46	67
F'		$N=0.520$[d]			298.2	0.7	0.951	2408				
WF	352	141.3[e]	1.0	1.23	251.7	0.7	0.977	2405	77	7.7	52	32
WF'		141.0[e]	1.0	1.23	280.5	0.7	0.977	2462				
E-18	352	10	1.291	0.725	23.4	1.191	0.599	1949	75.5	7.6		
E-18'		10	1.295	0.665	23.4	1.194	0.591	1947				
A	352	100	0.971	0.652	44.1	1.043	1.051	2699	81	8.1	59	38
A'		100	0.951	0.720	44.1	1.076	0.963	2595				
S	352	50	1.077	0.641	43.0	1.041	1.004	2564	78	7.8	61	16
S'		50	1.054	0.733	43.0	1.072	0.849	2311				
F	56	$N=0.973$[d]			14.6	1.2	0.779	1476	25	8.8		
WF	56	286.0[e]	1.0	1.23	13.4	1.2	0.707	1371	25	8.8		
E-18	56	10	1.383	0.571	23.4	1.2	0.709	1493	25.5	9.0		
S[f]	56	50	1.093	0.743	43.0	1.093	0.743	1494	25	8.8		
E-18[g]	33-215	10	1.35	0.618	23.4	1.23	0.552					

[a] $R_i=r_i(18^{1/3}+28^{1/3})=5.657r_i$.

[b] L_F is the angular momentum (rounded to the nearest 0.5) for which $d\,|\,S_L\,|\,/dL$ is maximum, D_F is the distance of closest approach on the Rutherford trajectory with $L=L_F$.

[c] Partial wave and scattering angle at which the nuclear rainbow occurs in scattering by the real part of the potential.

[d] Renormalization of the real folded potential: see text.

[e] The real potential is Woods-Saxon squared.

[f] Potential constrained to have $r_W=r_V$, $a_W=a_V$.

[g] Potential for ^{16}O+^{28}Si scattering from Ref. 6.

lowed to increase slowly and linearly with energy. These potentials were *not* surface transparent.

It should also be noted that the ^{16}O data used in those studies were confined to scattering angles in the forward hemisphere ($\theta_{c.m.} \lesssim 30°$ at 215 MeV). At the highest energies, these angles are too small to reveal evidence of any "farside dominance" or rainbow phenomena that might distinguish between the various potentials.[11,17] Further, those analyses ignored the oscillations which were beginning to appear for $\theta_{c.m.} \gtrsim 60°$ in the data for $E \sim 50$ to 70 MeV. These oscillations are now known[8] to extend to 180°—the so-called anomalous large angle scattering (ALAS) phenomenon—at least for bombarding energies in the range $30 \leq E \leq 55$ MeV. These angular distributions have been fitted by use of a variety of optical potentials, including one whose real part is a deep, folded one with some surface modifications.[9] An important characteristic of these potentials is a surface transparency that decreases with increasing energy.

The earlier ^{18}O data at 56 MeV considered here, and shown in Fig. 4, are also confined to forward angles ($\theta_{c.m.} < 90°$), where the scattering is less sensitive to details of the potentials and ambiguities remain in the optical-model analyses. In the present study, first an optical-model analysis of the 352 MeV data with different forms of potentials was applied only to the initial measurements where $2.6° \leq \theta_{lab} \leq 14.1°$. Later, further optical-model searches were performed using the extended data at larger angles to investigate whether additional information could be obtained on the nature of the appropriate optical potential.

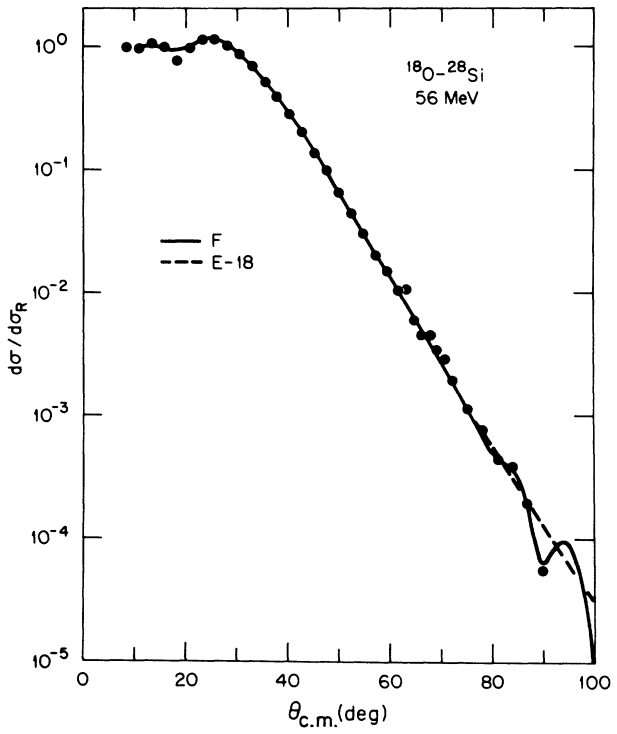

FIG. 4. Comparison between measured elastic scattering at 56 MeV with optical-model fits obtained with the folding model potential F and potential E-18 of Table I. The predictions for the Woods-Saxon-squared potential WF are essentially identical to those for the folding model, while the angular distribution from potential S is very similar to that from E-18.

We chose to pursue three types of WS potential obtained from ^{16}O studies, the shallow, surface transparent E-18 type,[6] the deeper ($V = 100$ MeV) A-type,[7] and the intermediate ($V = 50$) S-type,[18] as well as a folded potential obtained using the $M3Y$ interaction[16] and the square of a Woods-Saxon potential that is equivalent to it. The data were fitted using the optical-model search program PTOLEMY;[19] representative results are shown in Figs. 2 and 3. We should note that the fits to the 352 MeV data are not perfect (as indicated by typical values for χ^2 of 3 to 5 per datum when uniform uncertainties of 10% are assumed). The cross sections at the three most forward angles are not reproduced correctly, while the structures in the angular distribution that are predicted near 8° and 10° are a little out of phase with those observed. Coupled-channels effects (Sec. IV) do not seem to remove these discrepancies.

B. Folded real potential

The real potential was obtained by folding the $M3Y$ effective nucleon-nucleon interaction[16] into the density distributions of ^{18}O and ^{28}Si. The latter was taken to be twice the shell-model proton distribution determined from electron scattering,[20] while model B' of Ref. 6 was used for ^{18}O. A phenomenological WS imaginary potential of the form (3.1) was included, as well as the Coulomb potential between two uniform charge distributions[19] of radii 3.68 and 4.05 fm, respectively. The real potential was multiplied by a renormalization constant N; this and the imaginary potential parameters were varied for an optimum fit to the data in the angular range 4.8° to 23.1°, with the usual χ^2 criterion.[19] A value of $N \approx 1.0$ would signify the validity of the folding model. The resulting parameters are labeled F in Table I. The precise values of the imaginary radius parameter were ambiguous, although clearly r_W needed to be smaller at the higher energy. To stabilize the searches, we fixed $r_W = 0.7$ fm at 352 MeV and $r_W = 1.2$ fm at the lower energy. Potential F' was obtained when the data between 23° and 29° were included in the fit.

A fit to the 56 MeV data, shown in Fig. 4, is easily obtained with $N \approx 1$. (Similar results with N close to unity were found previously[16] for other ^{18}O+^{18}Si data in this energy region.) However, fits to the 352 MeV cross sections (which are comparable to those obtained for potential S shown in Fig. 2) can only be obtained with the real potential reduced in strength by a factor of 2 ($N \approx 0.52$).

This strong energy dependence appears to be in striking contrast to the global ^{16}O scattering results of Ref. 7 where a constant N was used from $E = 33$ to 215 MeV. When corrected for small differences in the interaction used in that work, its value corresponds to $N \approx 0.8$ here. However, best fits obtained[16] at individual energies do show a comparable energy dependence in N. At the lower energies, the optimum $N \approx 1.0$ is found, but this has decreased to $N \approx 0.91$ at 142 MeV and $N \approx 0.76$ at 215 MeV. A linear extrapolation to 352 MeV gives

$N \approx 0.5$, just as is found here for the ^{18}O scattering. This is illustrated in Fig. 5.

Such a strong energy dependence was not seen for other heavy-ion systems.[16] A reduction in N from unity was seen[21] for ^{40}Ar scattering at 44 MeV/nucleon, but only to $N \approx 0.7$, when the same folding model was used. This energy is more than twice the 20 MeV/nucleon of the present experiment. A density-dependent development[21] of the $M3Y$ effective interaction, called $DDM3Y$, varies with energy much more strongly than the original $M3Y$ one, and has been shown[22] to reproduce $^{12}C+^{12}C$ and $^{16}O+^{12}C$ scattering for energies E/A from 9 to 94 MeV. The same model gives a good account[23] of $^{16}O+^{28}Si$ scattering at $E/A=94$ MeV, but when applied to this system at lower energies, or to the present $^{18}O+^{28}Si$ data, it still requires renormalization factors N not very different from those needed for the original $M3Y$ interaction. Similar discrepancies were found[21] for other heavy-ion systems in this low-to-intermediate energy region.

C. Woods-Saxon-squared potential

The folded real potential in the surface region can be represented closely by the square of the WS form (3.1). We continue to use the standard WS function for the imaginary part. Then we have

$$U(r) = -V[f(x_v)]^2 - iWf(x_W) \ . \tag{3.2}$$

The values $V=270$ MeV, $r_v=1.0$ fm, and $a_V=1.23$ fm then fit the folded potential over the important radial region $r \approx 6$ to 12 fm, where $-V$ ranges from 55 MeV to 10 keV. In order to fit the scattering data, we kept this shape fixed, but varied the real depth V, corresponding to the variation of N in the folding model. The resulting potentials WF and WF′ in Table I, correspond to fits to the limited and extended data, respectively. They yield almost exactly the same scattering as the respective F-type potentials, while their strengths V correspond closely to the $N(56) \approx 1$, $N(352) \approx 0.5$ found for them. Thus these $(WS)^2$ potentials may be used as convenient analytical substitutes for the numerical folded potential. No clear improvement in reproducing the data was noticed with the new F' (or WF′) potentials in comparison to the original F (or WF) potential fits.

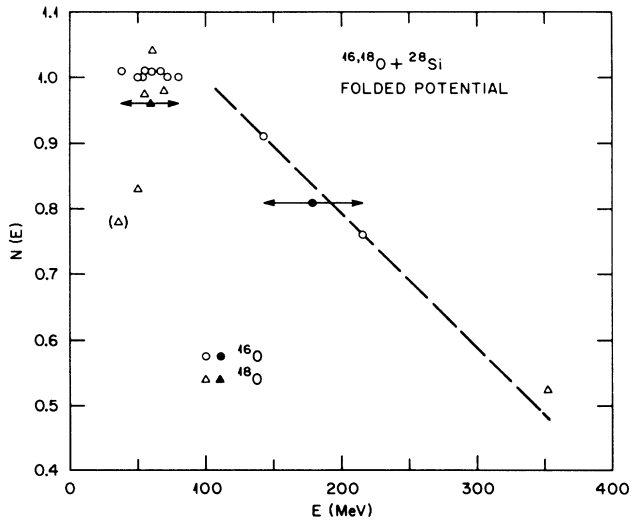

FIG. 5. Renormalization factors $N(E)$ for the real folded potentials with the $M3Y$ interaction, needed to fit ^{16}O and ^{18}O scattering from ^{28}Si at various bombarding energies E. The solid circle and solid triangle correspond to global fits to data over the indicated energy range. The dashed line represents a linear extrapolation of the results for ^{16}O at 142 and 215 MeV.

D. Woods-Saxon potentials

Here we use the standard potential form of Eq. (3.1). We started from three types of potential that had been obtained in earlier work: the A-type[7] with $V=100$ MeV, the S-type[18] with $V=50$ MeV, and the surface-transparent E-18 type[6] with $V=10$ MeV. The S-type potential had been obtained from analysis of elastic and transfer data for $^{18}O+^{28}Si$ at 56 MeV incident energy. For each of these types, automatic searches were made varying different combinations of the geometric parameters: $(r_V=r_W, a_V, a_W)$, $(r_V, r_W, a_V=a_W)$, and (r_V, r_W, a_V, a_W), keeping V, W fixed in each case. Very similar values of χ^2 were obtained ($\chi^2 \simeq 4-5$ per datum assuming a uniform 10% uncertainty for each experimental cross section) for the fits resulting from these different searches and potential families. We found that varying the value of W as well led to instability in the search procedure.

In Table I are shown the parameter values derived by varying all four of the geometric parameters independently. The first of each pair listed for each type of potential resulted from fits to the initial, limited ($\theta_{c.m.} \lesssim 23.15°$) measured elastic cross sections, while the second (primed) set was obtained from the extended measurements ($\theta_{c.m.} \lesssim 29.05°$). In Fig. 2 we show the comparison of the restricted data with optical-model predictions using the three types of potential. A discrimination between the different potentials is not possible. The amplitudes of the oscillations in the angular distributions predicted by all the potentials increase until $\theta_{c.m.} \approx 20°$. Beyond this angle, the E-18 oscillations remain roughly constant, while those for the other potentials decrease in amplitude. Especially striking is the very deep and narrow minimum near 20° exhibited by each except the E-18. We return to these characteristics in Sec. III G. Figure 3 shows that even extending the data to $\theta_{c.m.} \sim 29°$ did not enable us to establish the nature of the optical potential. Fits with comparable χ^2 show noticeable deficiencies in different angular regions.

E. Characteristics of the potentials

Later we show evidence that the scattering at 352 MeV is only sensitive to the potential for separations $r \gtrsim 6$ fm. In this region, the A and S potentials are almost identical, while the F and WF potentials are very similar to them. As Fig. 6 illustrates, these potentials are characterized by $|\,\mathrm{Im}U\,| \rangle |\,\mathrm{Re}U\,|$ for $r \gtrsim 7$ fm. The E-18 potential shows quite the contrary behavior; the absorptive part is weaker than the real, refractive part for $r > 7.8$

fm, but stronger at smaller radii. This "surface transparency," which is a general feature of E-18 type potentials,[6,10] is important for understanding the scattering that they induce.[11] It also results, at this energy, in a reaction cross section σ_A which is some 20% smaller than those calculated for the other types of potentials (Table I).

The dashed curve in Fig. 4 shows the E-18 type fit to the data[10] taken at 56 MeV. It shows no oscillations beyond 30°, although it is interesting to note that an apparently similar E-18 type of potential used in a coupled-channels treatment[10] did result in oscillations at the larger angles similar to those seen here (Fig. 4) for the folded potential F. However, closer inspection shows that, while the imaginary parts of these two E-18 type potentials are almost identical, the real part of the one (with $V=19$ MeV) from Ref. 10 is approximately twice the strength of ours at all radii and hence leads to more refraction in the surface region. Indeed our E-18 potential at 56 MeV does not show a marked surface transparency like that seen (Fig. 6) at 352 MeV; its real and imaginary parts are roughly equal for peripheral collisions.

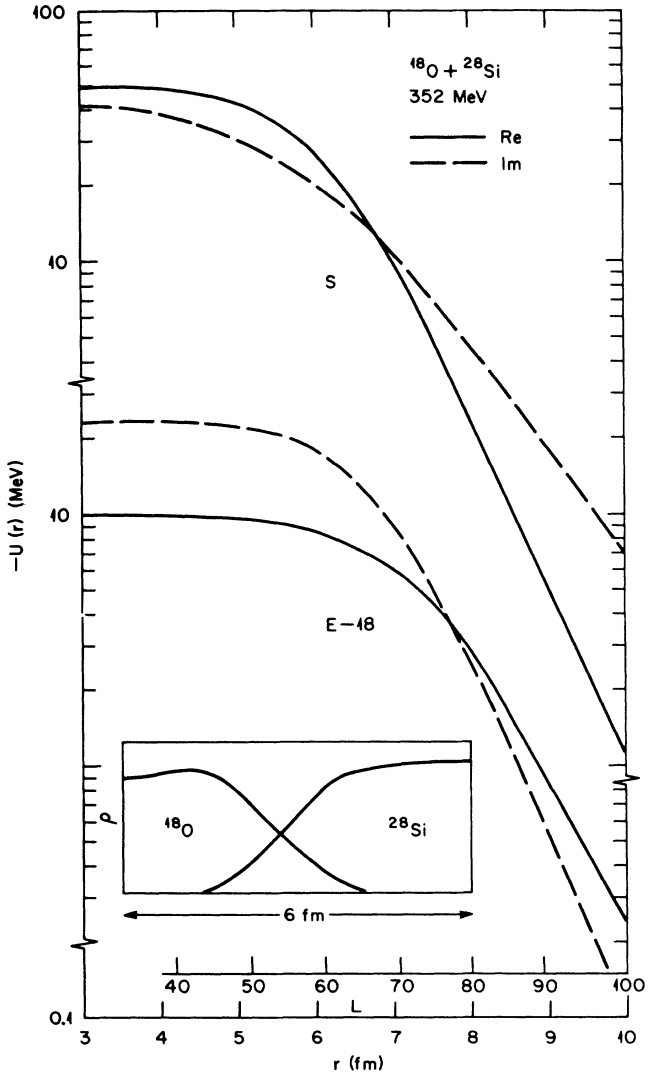

FIG. 6. The optical potentials S and E-18 for $^{18}O+^{28}Si$ at 352 MeV. The parameter values are given in Table I. At the bottom is a scale showing the partial wave number L for which the corresponding Rutherford orbit has r as its distance of closest approach. The inset shows the density distributions of the two nuclei when their centers are separated by 6 fm.

The S-type fit[18] to the 56 MeV data is like that shown in Fig. 4 for E-18. This S potential differs from the corresponding one found at 352 MeV (Fig. 6) in that its real and imaginary parts were constrained to have the same shape; consequently the imaginary-to-real ratio is 0.86 at all radii. Other searches in which the two parts were allowed to have different shapes did result in this ratio being reduced in the surface region. The increased transparency in the surface then led to oscillations appearing at the larger angles. This improved the agreement with the data in this angular region, and reduced the overall χ^2, but at the expense of poorer agreement at small angles where the cross sections are oscillating about the Rutherford values. For this reason, we preferred the constrained potential whose parameter values are included in Table I.

F. Comparison of results at 56 and 352 MeV

The analyses at both energies are subject to considerable ambiguities. Some general features can be discerned when the optical-model results for the two energies are compared. The real potential in the important surface region ($r \approx 8-9$ fm, say) needs to be roughly twice as strong at the lower energy. This is seen most clearly for the $M3Y$ folding model which gives the same shape at both energies but needs to be renormalized by $N \approx 0.54$ at 352 MeV, whereas $N \approx 1$ is satisfactory at 56 MeV. This is similar to the results found for $^{16}O+^{28}Si$ (Fig. 5). The S-type potentials show the same trend. The effect is less marked for the E-18 type, but still present.

The other feature noticeable from Table I, except for the E-18 type, is that the imaginary diffuseness a_W needs to be appreciably larger at the high energy. This is also reminiscent of the behavior found[7] for $^{16}O+^{28}Si$ scattering, where $a_W \sim 1$ fm was required at the highest energies. The effect is reversed, however, for the E-18 potential. An energy dependence of the imaginary potential is not unexpected;[24] it has been seen clearly at low energies,[9] but it is not known what form it might take at an energy as high as 352 MeV.

G. Partial-wave decomposition

The elastic scattering matrix is $S_L = |S_L| \exp(2i\delta_L)$, where δ_L is the (real) phase shift and L denotes the Lth partial wave with angular momentum $\lambda \approx L + \frac{1}{2}$ in units of $\hbar$. It is convenient[2] to write it in terms of its modulus $\eta(\lambda) = |S_{L=\lambda-1/2}|$ and the quantal deflection function $\Theta(\lambda) = 2(d\delta_L/dL)_{L=\lambda-1/2}$. The departure of $\eta(\lambda)$ from unity is a measure of the absorption for that partial wave, while the observed scattering angle is $\theta = |\Theta|$. Because the identification of $\Theta(\lambda)$ with the classical deflection function is no longer strictly valid when the potential is complex, it is more meaningful to consider[17,25] the $\Theta(\lambda)$

generated by scattering from the real part of the potential alone (i.e., with $W=0$). Examination of the absorption profiles $\eta(\lambda)$ and the deflection functions $\Theta(\lambda)$ gives further insights into the nature of the various potentials that fit a given set of data.

The moduli $\eta(\lambda)$ for the 352 MeV potentials are shown in Fig. 7. The lower scale indicates the distance of closest approach $D(\lambda)$ for the Rutherford trajectory with angular momenta λ. The classical trajectories $D \gtrsim 6$ fm are perturbed very little by the nuclear potentials, so that this scale gives some indication of the radial region in which the potentials are being sampled. All the potentials except E-18 result in total absorption, $\eta(\lambda)\approx 0$, for $\lambda \leq 60$ (and hence $D \lesssim 6$ fm), and 99% absorption ($1-\eta^2=0.99$) for $\lambda \approx 70$ ($D \approx 7$ fm). As the inset to Fig. 6 shows, $D=6$ fm already represents considerable overlap of the density distributions of the two interacting nuclei. Scattering by the E-18 potential samples slightly smaller radii. The "surface transparency" of E-18 is manifest by $\eta(\lambda)$ for the potential being appreciably larger in the "surface" region $60 \lesssim \lambda \lesssim 110$, or 6 fm $\lesssim D \lesssim 11$ fm. This behavior reflects the relative strengths of the corresponding absorptive potentials in the surface region (see Fig. 6). We have shown elsewhere[4] that these differences in $\eta(\lambda)$ have important consequences for a distorted-waves treatment of nucleon transfer reactions. We note also that the absorption profile for the other potentials are not identical, F being least absorptive. This fact emphasizes that surface transparency is not necessarily correlated with a "shallow" potential, if by this is meant the depth of the potential at small radii (the value of V for WS or WS^2 potentials). The F potential is nearly 400 MeV deep at $r=0$, but it is the potential value in the surface that determines the character of the scattering.

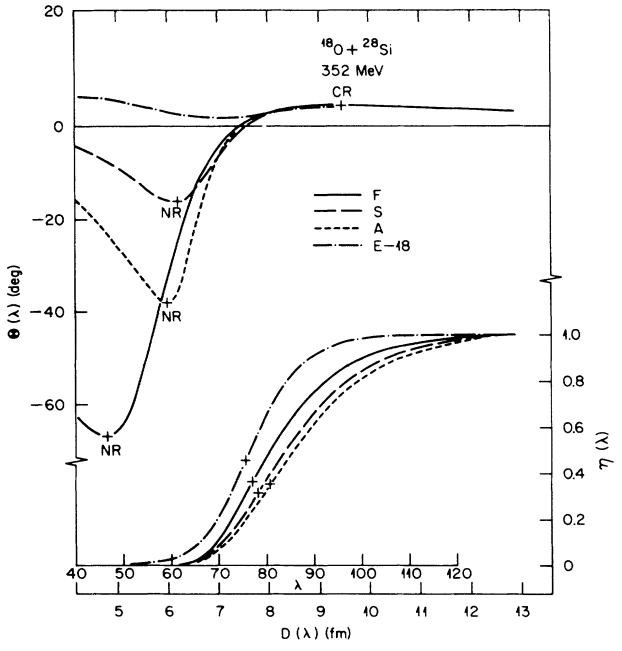

FIG. 7. The moduli $\eta(\lambda)=|S_L|$ for $\lambda=L+\frac{1}{2}$ of the partial-wave scattering matrix elements for some of the 352 MeV potentials given in Table I. [The $\eta(\lambda)$ for the WF potential is almost identical with that for potential F.] The crosses (+) mark the "strong absorption" λ_F for which $d\eta(\lambda)/d\lambda$ is a maximum. Also shown are the deflection functions $\Theta(\lambda)=2(d\delta_L/dL)$, evaluated at $L=\lambda-\frac{1}{2}$, for scattering by the real parts of these potentials. The notation NR denotes the nuclear rainbow and CR means Coulomb rainbow. The lower abscissa scale shows the distance of closest approach $D(\lambda)$ for a classical Rutherford trajectory with angular momentum $\lambda\hbar$. Note the suppressed zeros on the abscissa scales.

Also marked in Fig. 7 are points at which $d\eta(\lambda)/d\lambda$ has a maximum for each potential. The corresponding λ_F closely approximate the critical $\lambda=\Lambda$ defined by Frahn,[2] and the associated $D(\lambda_F)$ play the role of strong absorption radii. Their values are included in Table I. The partial-wave contributions to peripheral, nonelastic direct reactions tend to peak for $\lambda \approx \lambda_F$ provided the reactions are reasonably well matched kinematically.[4]

The deflection functions $\Theta(\lambda)$ for scattering by the real parts of the potentials are shown in the upper part of Fig. 7. They are all very different, but, except for E-18, these differences are only large for those values of λ for which $\eta(\lambda)$ is very small. That is, the strong absorption for $\lambda \lesssim 70$ prevents the differences in the $\Theta(\lambda)$ from being observed. In particular, although the real part of each of the deeper potentials has the capacity to produce a "nuclear rainbow" [points for negative $\Theta=\Theta_{NR}$ at which $d\Theta(\lambda)/d\lambda=0$], such rainbows never appear in the actual scattering.[17,25] The real part of the E-18 potential is too weak to give rise to any negative angle scattering (in the classical sense) although it exhibits a very weak rainbow with $\Theta \approx 2°$ and $\lambda \approx 70$.

All the potentials give rise to a "Coulomb rainbow".[1] At 352 MeV it occurs with $\Theta_{CR}\approx 4°$ at $\lambda=100$ for the E-18 potential and $\lambda \approx 96$ for the other potentials.

Thus we see from these various results that the E-18 type of potential, and the other, deeper ones, represent two distinct ways of interpreting the available data in terms of scattering with different physical characteristics. These differences are further emphasized in the next section, and are very similar to those found for the $^{16}O+^{28}Si$ system.[11]

H. Farside/nearside decompositions

The deflection functions $\Theta(\lambda)$ just discussed imply that the potentials, except the E-18, can sustain negative-angle, or farside scattering. However, the absorption profiles $\eta(\lambda)$ indicate that particles which traverse classical trajectories that are deflected to negative angles $\Theta < -10°$ are strongly absorbed; these angles are in shadow. Quantitatively, wave diffraction at the edge of the absorptive region allows leakage into this shadow with an intensity that falls in a roughly exponential way with increasing angle. The presence of an attractive real potential in the surface enhances this farside scattering, reducing the slope of the exponential decay.

Similarly, although nearside scattering (i.e., to positive Θ) is not classically allowed for $\Theta \gtrsim 4°$, diffraction allows larger angles to be illuminated, again with an intensity that falls exponentially. In this case, the attractive potential resists scattering to the larger angles, causing the ex-

ponential decay to be steeper.

These ideas are formalized[2,11,17] in an exact decomposition of the scattering amplitude into farside (F) and nearside (N) components, $f(\theta)=f_N(\theta)+f_F(\theta)$. This was done for the potentials obtained in the present work; two examples are shown in Fig. 8. Plotted are the quantities $\ln[2\pi\sin(\theta)\sigma(\theta)]$, where for the nearside alone, $\sigma(\theta)=\sigma_N(\theta)=|f_N(\theta)|^2$, for the farside alone, $\sigma(\theta)=\sigma_F(\theta)=|f_F(\theta)|^2$, and for their coherent sum, $\sigma(\theta)=|f(\theta)|^2$.

The F, WF, and S potentials give results qualitatively similar to those shown for A in Fig. 8. At small angles, the nearside scattering is dominant, but the attractive nuclear potential, gives σ_N and σ_F different slopes, so that eventually they are equal. This crossover occurs for a scattering angle $\theta\approx 20°$ for these potentials, and their interference produces a very deep minimum near that angle. The interference oscillations die out on either side of the crossover angle. The farside dominates at larger angles and the angular distribution assumes a smooth falloff.[11,17]

In the absence of absorption, interference between the two components of the farside amplitude that contribute for a given deflection when $0>\Theta>\Theta_{NR}$, corresponding to the two branches of the deflection function (see Fig. 7), would have produced the Airy maxima and minima that characterize a rainbow.[17] This is illustrated in Fig. 8 where the farside cross section calculated for potential A but with $W=0$ is also shown. Potentials S, F, and WF also show rainbows in their farside amplitudes when we put $W=0$, but with different rainbow angles Θ_{NR} (Fig. 7 and Table I). Thus the farside cross section for potential F, with $\Theta_{NR}=-67°$, shows Airy oscillations over the whole angular region studied here, whereas that for potential S, with $\Theta_{NR}=-16°$, only shows the last Airy minimum before the primary rainbow maximum, at $\theta\approx 2°$. In any case, absorption has removed any traces of these rainbow patterns of the farside scattering from the full, complex, potentials. Such rainbows cannot be observed and we are left with simple farside dominance.[17]

The E-18 potential provides quite a different behavior. After nearside dominance at small angles, the near and far components fall roughly parallel, so that their interference pattern continues with oscillations of approximately constant amplitude. The very similar results for $^{16}O+^{28}Si$ scattering at 215 MeV with this type of potential have been interpreted[11] in terms of a "black ball enclosed in a glass casing" and that same discussion is valid here.

The inclusion of the data extending out to $\theta\sim 29°$ drives the search to potentials with a near/far crossover in the range $\theta\sim 22°-26°$, even with the E-18 type. The behavior of the near/far components for the E-18′ potential is similar to the E-18 case shown in Fig. 8 except that the near branch does not bend upward for $\theta\gtrsim 20°$ and the far-branch falls off a little less steeply, resulting in a crossover near $\theta=23°$. Since the near and far amplitudes for E-18′ do not diverge rapidly for angles beyond the crossover, their interference oscillations continue just like they do for E-18 in Fig. 8, but now with the farside one dominant.

These results imply that the two kinds of scattering ex-

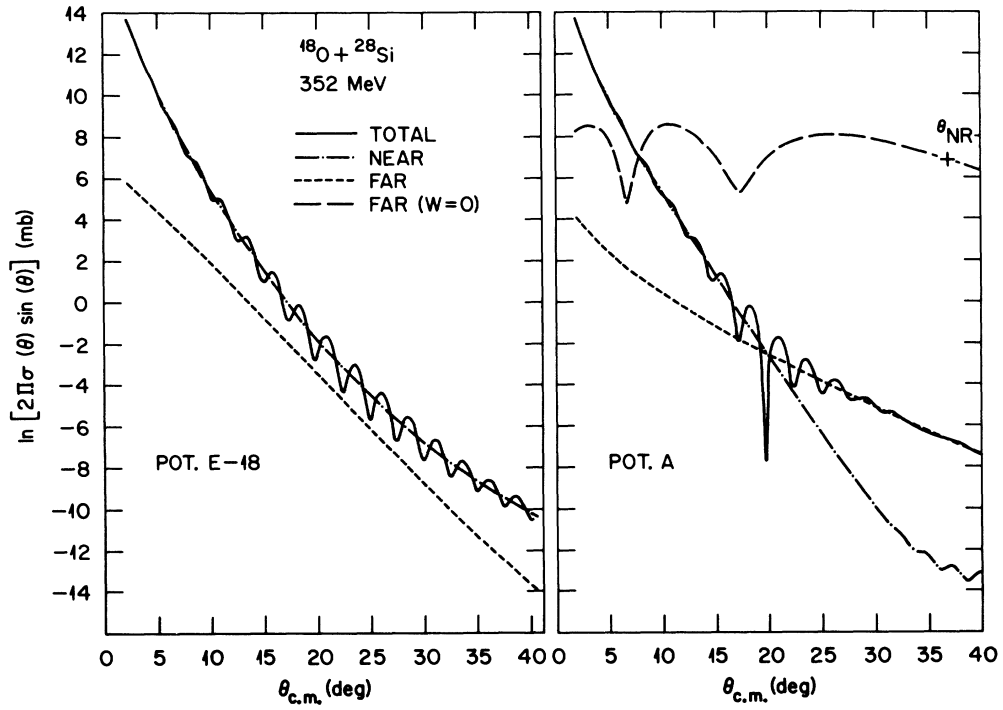

FIG. 8. Nearside/farside decomposition of the scattering at 352 MeV by potentials A and E-18. Also shown is the farside cross section for scattering by the real part of potential A without absorption ($W=0$); Θ_{NR} on this curve indicates the nuclear rainbow angle obtained from Fig. 7.

hibited in Fig. 8 could be distinguished unambiguously by precise measurements of the cross sections for scattering angles out to 40°, say. The present data are still insufficient to allow a choice to be made between different potentials. (A similar ambiguity remains for $^{16}O+^{28}Si$ scattering, where the measurements also stop close to the near-far crossover angle predicted by the deeper potentials.)

I. Summary of elastic analysis

Despite the extension of the elastic measurements out to 29° the optical-model analysis remains ambiguous, and the results obtained are very similar in character to those found for $^{16}O+^{28}Si$ scattering at 215 MeV. However, the allowed potentials fall into two categories. The first, represented by the E-18 type, are surface transparent. All potentials imply that nearside scattering is dominant for $\theta \lesssim 20°$, but the E-18 type predicts that nearside dominance continues to larger angles. (The E-18′ that results when the extended data are included, does have a near-far crossover, but otherwise the characteristics of the scattering by this potential remain similar to those for E-18.) The second category is comprised of more strongly absorbing potentials but whose real parts are sufficiently attractive in the surface that farside scattering dominates for $\theta > 20°$. Including the elastic data for the larger angles results in potentials for which the near-far crossover occurs at slightly larger angles. The deflection functions for scattering by the real parts of the E-18 type potential give no indication of a nuclear rainbow, whereas the potentials of the second category do. However, the strong absorption that is present for low partial waves eliminates all trace of such rainbows in the actual scattering.

We shall see in the next section that these conclusions are not changed when the effects of couplings to inelastic channels are included explicitly by doing coupled-channels calculations.

IV. ANALYSIS OF INELASTIC SCATTERING

Cross sections were extracted for the excitation of the lowest 2^+ states in the projectile (1.98 MeV) and the target (1.78 MeV), as well as for the 6.88 MeV excitation, assumed to be due to a known 3^- state[10,26] in ^{28}Si. These are shown in Figs. 9 and 10. The strongest group was that for excitation of the 2^+ in ^{28}Si, and preliminary calculations indicated that the distorted-wave Born approximation[3] was not adequate for its analysis. Coupled-channels calculations[3] were made using the program PTOLEMY.[19]

A. The 2^+ excitation in ^{28}Si

There is evidence[27] that, to some approximation, the nucleus ^{28}Si can be regarded as an axially symmetric, oblate, rotor. We adopted that model and introduced the deformation into the corresponding Woods-Saxon optical potential (3.1) in the usual way,[1,3] $U(r) \rightarrow U(r,\theta)$, by defining radii in the body-fixed frame of axes,

$$R_i \rightarrow R_i + \delta_\lambda^N Y_\lambda^0(\theta) , \tag{4.1}$$

where $i=V$ or W for the real and imaginary parts, respectively. The radial parts of the corresponding 2^λ-pole coupling potentials were then obtained by projection,[3]

$$U_\lambda(r) = 2\pi \int U(r,\theta) Y_\lambda^0(\theta) \sin\theta d\theta . \tag{4.2}$$

Only the quadrupole, $\lambda=2$, term was included here. Coulomb excitation was included using 360 partial waves, although its effect is small except at the most forward angles. Also, this 2^+ state is known[27] to have a large, positive quadrupole moment, so allowance was made for its reorientation by both nuclear and Coulomb couplings. A recent evaluation[28] gives $B(E2)=326\ e^2\text{fm}^4$ for this transition, and this value was used. In the symmetric, oblate, rotor model this implies a quadrupole moment for the 2^+ state of $+16.4\ e\ \text{fm}^2$, compared to the measured[27] value of $+17.5\pm2.9\ e\ \text{fm}^2$.

We expect[3] the potential deformation length δ_2^N in Eq.

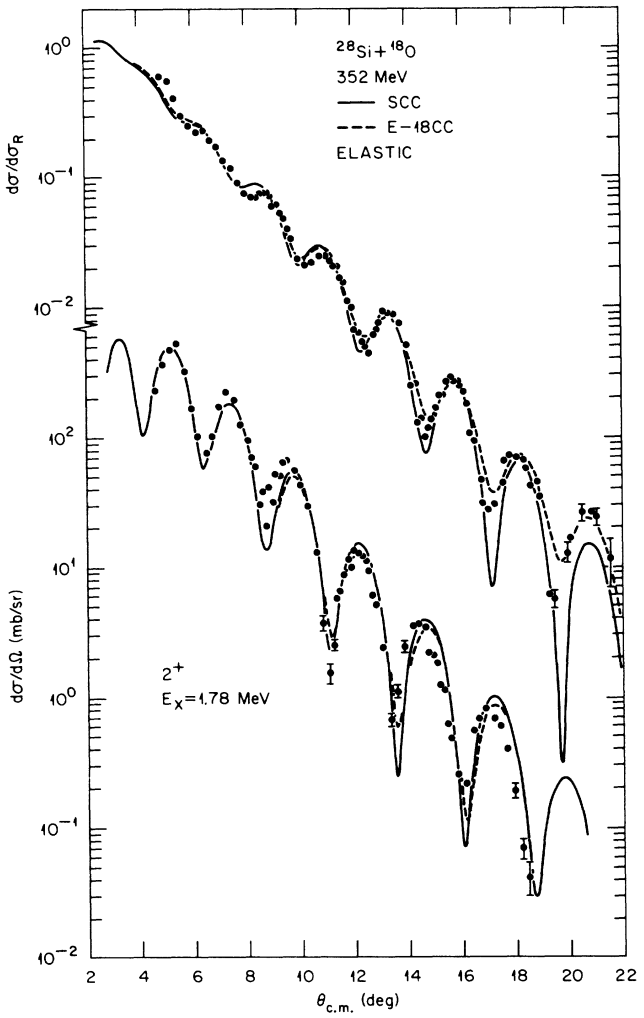

FIG. 9. Differential cross sections for the elastic scattering and for the excitation of the 2^+ state of ^{28}Si. The curves are the results of coupled-channels calculations treating ^{28}Si as an oblate rotor with a potential deformation length $\delta_2^N=-1.2$ fm. The potentials *SCC* and *E*-18*CC* correspond to potentials S' and E-18′ of Table I except for reductions in the values of a_W ($a_W=0.73$ fm for *SCC*, $a_W=0.535$ fm for *E*-18*CC*).

(4.1) to be comparable to the corresponding deformation length δ_2^C of the ^{28}Si charge distribution deduced from the measured $B(E2)$ value for this transition. If we assume that the ^{28}Si charge distribution[29] has a Woods-Saxon shape with $R_c=3.14$ fm, $a_c=0.536$ fm, and that the transition charge density is given by deforming this, using the same procedure as in Eqs. (4.1) and (4.2), we deduce $\delta_2^C\approx -1.2$ fm (oblate) or $+1.6$ fm (prolate). However, electron scattering measurements[29] indicate that the transition charge density deviates somewhat from the shape given by this prescription, so that we cannot expect a precise correspondence between optical-model and charge deformation lengths.

Studies were made based upon all three types of Woods-Saxon potentials E-18′, A', and S', listed in Table I. The feedback of the coupling onto the elastic scattering mostly results in a dampening effect, causing the elastic differential cross sections to fall off somewhat faster with increasing angle compared to the one-channel cases discussed earlier. We looked for the simplest adjustment that could be made to the optical potential parameters listed in Table I that would restore the agreement with the elastic scattering measurements when used in a 0^+-2^+ coupled-channels calculation. Frequently it is assumed that a small reduction in the strength W of the imaginary potential will be sufficient, but we found that the optimum one-parameter variation was a reduction of 10–15 % in the imaginary diffuseness a_W. Reducing a_W also reduces the rate of fall with increasing angle of the inelastic cross sections. The remaining adjustable parameter is the potential deformation length δ_2^N. Both the magnitudes of the inelastic cross sections, and the degree of dampening of the elastic cross sections, are roughly proportional to $(\delta_2^N)^2$. Consequently the variations in a_W and δ_2^N allowed by the data are correlated. The curves shown in Fig. 9 were obtained by choosing $\delta_2^N=-1.2$ fm, as suggested by the measured $B(E2)$, and associated a_W values of 0.535 fm for potential E-18CC (a 10% reduction from $a_W=0.591$ fm for E-18′) and 0.73 fm for potential SCC (a 14% reduction from $a_W=0.849$ fm for S'). Comparable fits were obtained with $\delta_2^N=-1.2$ fm by replacing $a_W=0.963$ fm for the A' potential by $a_W\approx 0.83$ fm.

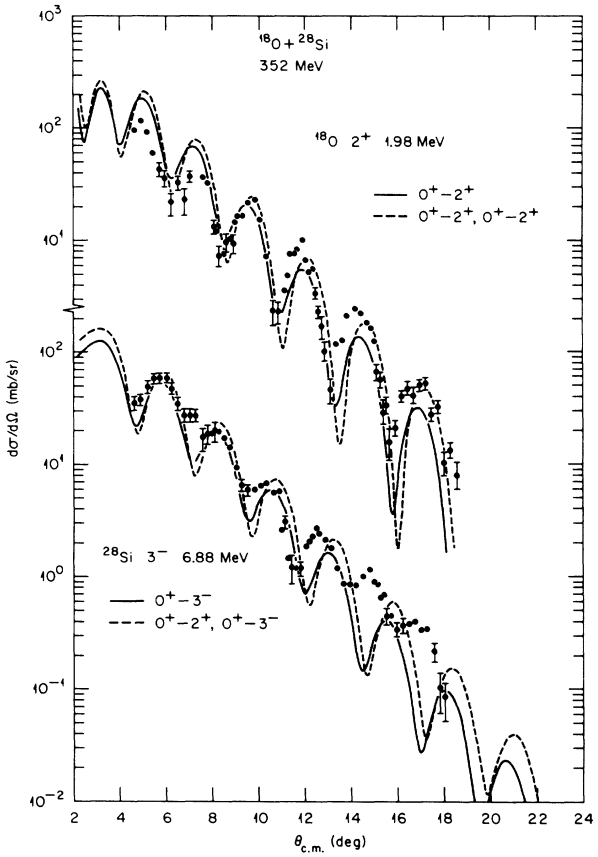

FIG. 10. Differential cross sections for the excitation of the 2^+ state in ^{18}O and the 3^- state in ^{28}Si. The curves were obtained from coupled-channels calculations, assuming in each case a simple harmonic vibration, with a potential deformation length of $\delta_2^N=0.72$ fm or $\delta_3^N=0.64$ fm. The solid curves correspond to using the S' optical potential and coupling only the ground state and the particular excited state. The dashed curves result from using the SCC potential and including also the coupling between the ground state and the 1.78 MeV 2^+ state of ^{28}Si.

The fits to the elastic data are comparable to those obtained with the one-channel optical potentials (Figs. 2 and 3, and Ref. 14) and have similar characteristics. For example, the S-type results in deeper minima than the E-18 type, and shows evidence for a far-near crossover near $\theta=20°$. In particular, the discrepancies noted earlier between the optical-model predictions and the data at the smaller angles are not removed by explicitly including the quadrupole coupling.

The agreement with the inelastic data is quite good for all three potentials, and is of similar quality to the elastic fits. More important is that all three require approximately the same deformation length, $\delta_2^N\approx -1.2$ fm, so that the magnitudes of the inelastic cross sections cannot be used to discriminate between the potentials. This is in striking contrast to the results for one-nucleon transfer reactions[4,12] where the surface-transparent E-18 type potential predicts cross sections as much as a factor of 3 larger than do the A or S types. The reason for this difference in behavior is easy to see. The coupling interaction responsible for the transfer reactions is essentially the same in all three cases (predominantly[3] the binding potential for the transferred nucleon), and only the distorted waves vary for the three potentials.[14] In contrast, use of the deformed potential model for inelastic scattering implies a strong correlation between elastic and inelastic processes,[2] the elastic and inelastic couplings being determined by the same potential. Then imposing the constraint that the elastic data be fit tends to result in similar inelastic cross sections.

Some other characteristics of the coupled-channels calculations may be noted. Within the rotational model, the results are dependent[3] upon the sign of δ_2. Repeating the calculations just discussed, but with a positive (prolate) δ_2, gives inelastic cross sections of similar magnitude but with oscillations shifted forward in angle by about 3% (about $\frac{1}{2}°$ at 17°, or about one-fifth of the spacing between

successive peaks in this angular region). This shift arises mainly from the reorientation of the 2^+ state; switching off this coupling gives rise to very similar angular distributions for either sign of δ_2. [They are not identical because the projection (4.2) itself contains small contributions from $(\delta_2)^3$ and higher odd powers.]

Changing the sign of δ_2 also effects the elastic scattering, but in the opposite sense to the inelastic; a positive δ_2 moves the oscillations in the elastic scattering backward by about the same degree. Thus the present results may be said to provide further support for the hypothesis that ^{28}Si is an oblate rotor, to the extent that we reproduce both elastic and inelastic angular distributions with this assumption. Unfortunately, the quality of the fits does not allow us to make a stronger statement.

Frequently the multipole coupling is taken to be the first term in a Taylor expansion[1,3] of the projection integral (4.2),

$$U_\lambda^{(1)}(r) = -\delta_\lambda^N dU(r)/dr \ . \tag{4.3}$$

This would be exact for the excitation of a single phonon of a 2^λ-pole harmonic shape vibration. We also made this assumption (with $\lambda=2$) for the 1.78 MeV 2^+ state of ^{28}Si (although it is inconsistent with the observation[27] of a large quadrupole moment for this state). Then we obtained differential cross sections that were very similar (in the angular region $\theta \lesssim 20°$ spanned by the data) to those shown in Fig. 9 for an oblate rotor, provided the value of δ_2^N was reduced by about 15%.

Finally, we note that the deformation of the imaginary optical potential plays a very important role in the excitation of this state. The imaginary part of the coupling dominates over the real part at all the angles studied ($\theta \leq 30°$), especially for the E-18 type potential. Further, the angular distributions produced by using either the real or the imaginary coupling by itself show oscillations with different periods, corresponding to the different "geometries" (especially the radii) of the associated potentials. It is their coherent sum which is responsible for the patterns seen in Fig. 9.

B. The 2^+ excitation in ^{18}O

In this case, the coupling (4.3) was used with $\lambda=2$; that is, the excitation was treated as a harmonic vibration. The value $B(E2)=45.1\ e^2\text{fm}^4$ was adopted.[28] If a Woods-Saxon shape with $R_c=2.525$ fm, $a_c=0.45$ fm is assumed for the ^{18}O charge distribution, and the prescription (4.1) is used, this corresponds to a deformation length $\delta_2^c=1.09$ fm.

Only the S'-type potentials were used. Two approaches were taken. In one, only this excitation and the ground state were coupled, using potential S' of Table I. The results for $\delta_2^N=0.72$ fm are labeled 0^+-2^+ in Fig. 10. In the other, the coupling between the ground state and the 2^+ state of ^{28}Si was included explicitly, and the modified S' potential ($a_W=0.73$ fm) was used. The results, obtained with the same δ_2^N, are labeled 0^+-2^+, 0^+-2^+ in Fig. 10. We see that the explicit inclusion of the ^{28}Si excitation has some effect on the angular distribution of the ^{18}O excitation, but it does not improve the agreement with the data. The measurements for $\theta \gtrsim 9°$ are consistent with $\delta_2^N \approx 0.7$–0.9 fm, but these values overpredict the cross sections for smaller angles. (Values of $\delta_2^N \approx 0.8$–0.9 fm were obtained for this transition upon analysis of ^{208}Pb + ^{18}O measurements[30] at 120 MeV.)

C. The 3^- excitation in ^{28}Si

A number of nuclei in this mass region exhibit[26] strong 3^- excitations with energies $\sim$6–8 MeV, including one in ^{28}Si at 6.88 MeV. We identify this with the strong group seen in the present experiment at 6.88 MeV (see Fig. 1). The quoted strength[26] corresponds to $B(E3)\uparrow = (3910 \pm 650)\ e^2\text{fm}^6$. This gives $\delta_3^c \approx (1.1 \pm 0.1)$ fm if a harmonic vibrator is assumed, with the prescription (4.1) and an rms radius[29] of 3.147 fm for the ground-state charge distribution.

The same procedure was used as for the 2^+ of ^{18}O; the S'-type potentials were used together with the vibrational coupling (4.3) with $\lambda=3$. Figure 10 shows the results with the coupling to the 2^+ state of ^{28}Si being included explicitly (labeled 0^+-3^-,0^+-2^+) and without this coupling (labeled 0^+-3^-). In both cases a potential octupole deformation length of $\delta_3^N=0.64$ fm was assumed. Coulomb excitation was included but has negligible effect. The most forward cross sections are reproduced fairly well, but the measured oscillations become out of phase with the theoretical ones at larger angles. The reasons for this discrepancy are not understood. There is a known[26] 4^+ level in ^{28}Si at 6.89 MeV, but there is no evidence that it is strongly coupled to the ground state, and its coupling via the 1.78 MeV 2^+ state is not particularly strong. Further, the results of some exploratory calculations along these lines did not suggest any simple explanation of the observed angular distribution.

V. CONCLUSIONS

We have presented results for the elastic and inelastic scattering of ^{18}O on ^{28}Si at 351.7 MeV ($E/A=19.54$ MeV). Optical-model analysis of the elastic measurements led to ambiguous results, with the allowed optical potentials falling into two categories which are either strongly absorbing or transparent in the surface region. The two types also exhibit very different deflection functions and give rise to scattering with different farside/nearside decompositions. Use of the folding model[16,21] for the real part resulted in potentials of the strongly absorbing type, while the real strengths had to be reduced by renormalization factors $N \sim 0.5$.

It has been demonstrated elsewhere[4,12] that the two categories of optical potential yield very different predictions for the magnitudes of one-nucleon transfer cross sections at this energy. In contrast, we have shown here that they predict cross sections of very similar magnitudes for the excitation of collective states by inelastic scattering, consequently these cannot be used to discriminate between the potentials. We interpret this difference in behavior in the following way. Our understanding[1,3] of strong excitations, expressed in our use of the collective (deformed potential) model, is that there is a strong

correlation between these inelastic amplitudes and the elastic ones.[2] This involves the use of a transition potential which is derived from the optical potential used, so that an ambiguity in the latter carries over to the former. The distorted-wave Born approximation description of transfer reactions, on the other hand, involves essentially the same transition interaction whatever the optical potentials, but the use of different optical potentials results in distorted waves with different characteristics.

Finally, we note that the various optical potentials do not result in *identical* scattering. There are small differences in the predicted angular distribution shapes, both for elastic and inelastic scattering, although they provide equivalent fits to the present data.

ACKNOWLEDGMENTS

We are indebted to M. J. Rhoades-Brown for making available the program PTOLEMY used in the optical-model analysis and to K. W. McVoy for providing the PNF version of that program that does the far-near decomposition of the amplitudes. This research was sponsored by the U.S. Department of Energy, under Contract DE-AC05-840R21400 with Martin Marietta Energy Systems, Inc.

---

*Present address: Instituto de Fisica, Universidade de São Paulo, São Paulo, Brasil.

†Deceased.

[1]R. A. Broglia and A. Winther, *Heavy Ion Reactions,* (Benjamin-Commings, Reading, Mass., 1981), Vol. 1.

[2]W. E. Frahn, in *Heavy-ion Science,* edited by D. A. Bromley (Plenum, New York, 1984), Vol. 1; *Diffractive Processes in Nuclear Physics* (Oxford University Press, Oxford, 1985).

[3]G. R. Satchler, *Direct Nuclear Reactions* (Oxford University Press, Oxford, 1983).

[4]D. J. Horen, M. A. G. Fernandes, G. R. Satchler, B. L. Burks, R. L. Auble, F. E. Bertrand, E. E. Gross, D. C. Hensley, R. O. Sayer, and D. Shapira, Z. Phys. A **328**, 189 (1987).

[5]G. Igo, Phys. Rev. **115**, 1665 (1959).

[6]J. G. Cramer, R. M. DeVries, D. A. Goldberg, M. S. Zisman, and C. F. Maguire, Phys. Rev. C **14**, 2158 (1977).

[7]G. R. Satchler, Nucl. Phys. **A279**, 493 (1977).

[8]P. Braun-Munzinger and J. Barrette, Phys. Rep. C **87**, 209 (1982); M. C. Mermaz, E. R. Chavez-Lomeli, J. Barrette, B. Berthier, and A. Greiner, Phys. Rev. C **29**, 147 (1984).

[9]A. M. Kobos and G. R. Satchler, Nucl. Phys. **A427**, 589 (1984).

[10]M. C. Mermaz, M. A. G. Fernandes, A. Greiner, B. T. Kim, and N. Lisbona, Phys. Rev. C **19**, 794 (1979).

[11]K. W. McVoy and M. S. Hussein, Prog. Part. Nucl. Phys. **12**, 103 (1984).

[12]M. A. G. Fernandes, B. L. Burks, D. J. Horen, G. R. Satchler, R. L. Auble, F. E. Bertrand, J. L. Blankenship, J. L. C. Ford, Jr., E. E. Gross, D. C. Hensley, R. O. Sayer, D. Shapira, and T. P. Sjoreen, Phys. Rev. C **33**, 1971 (1986).

[13]D. J. Horen, B. L. Burks, M. A. G. Fernandes, R. L. Auble, F. E. Bertrand, J. L. Blankenship, J. L. C. Ford, Jr., E. E. Gross, D. C. Hensley, R. O. Sayer, G. R. Satchler, D. Shapira, T. P. Sjoreen, and F. Petrovich, Phys. Lett. B **181**, 38 (1986).

[14]M. V. Hynes, J. L. C. Ford, Jr., T. P. Sjoreen, J. L. Blankenship, and F. E. Bertrand, Nucl. Instrum. Methods **224**, 89 (1984).

[15]T. P. Sjoreen, J. L. C. Ford, Jr., J. L. Blankenship, R. L. Auble, F. E. Bertrand, E. E. Gross, D. C. Hensley, D. Schull, and M. V. Hynes, Nucl. Instrum. Methods **224**, 421 (1984).

[16]G. R. Satchler, Nucl. Phys. **A329**, 233 (1979); G. R. Satchler and W. G. Love, Phys. Rep. C **55**, 183 (1979).

[17]K. W. McVoy and G. R. Satchler, Nucl. Phys. **A417**, 157 (1984).

[18]B. T. Kim, A. Greiner, M. A. G. Fernandes, N. Lisbona, K. S. Low, and M. C. Mermaz, Phys. Rev. C **20**, 1396 (1979).

[19]M. H. Mcfarlane and S. C. Pieper, Argonne National Laboratory Report No. ANL-76-11, Rev. 1, 1978 (unpublished).

[20]G. C. Li, M. R. Yearian, and I. Sick, Phys. Rev. C **9**, 1861 (1974).

[21]M. E. Farid and G. R. Satchler, Nucl. Phys. **A438**, 525 (1985).

[22]M. E. Brandan, *Proceedings of the 10th Oaxtepec Symposium on Nuclear Physics* (Instituto de Fisica, UNAM, Mexico City, 1987), Vol. 10, p. 1; and (in press).

[23]P. Roussel, N. Alamanos, F. Auger, J. Barrette, B. Berthier, B. Fernandez, L. Papineau, H. Doubre, and W. Mittig, Nucl. Phys. **A477**, 345 (1988).

[24]G. Pollarolo, R. A. Broglia, and A. Winther, Nucl. Phys. **A406**, 369 (1983); J. M. Quesada, R. A. Broglia, V. Bragin, and G. Pollarolo, *ibid.* **A428**, 589 (1984).

[25]K. W. McVoy, H. M. Khalil, M. M. Shalaby, and G. R. Satchler, Nucl. Phys. **A455**, 118 (1986).

[26]P. M. Endt, At. Data Nucl. Data Tables **23**, 3 (1979).

[27]G. C. Ball, O. Hausser, T. K. Alexander, W. G. Davies, J. S. Forster, I. V. Mitchell, J. R. Beene, D. Horn, and W. McLatchie, Nucl. Phys. **A349**, 271 (1980).

[28]S. Raman, C. H. Malarkey, W. T. Milner, C. W. Nestor, and P. H. Stelson, At. Data Nucl. Data Tables **36**, 1 (1987).

[29]S. W. Brain, A. Johnston, W. A. Gillespie, E. W. Lees, and R. P. Singhal, J. Phys. G **3**, 821 (1977).

[30]E. E. Gross, J. R. Beene, K. A. Erb, M. P. Fewell, D. Shapira, M. J. Rhoades-Brown, G. R. Satchler, and C. E. Thorn, Nucl. Phys. **A401**, 362 (1983).